TiNb$_2$O$_7$-Keratin derived carbon nanocomposites as novel anode materials for high-capacity lithium-ion batteries

Ganesh Babu Thiyagarajan [a,b], Vasu Shanmugam [c], Michael Wilhelm [d], Sanjay Mathur [a,b,d,**], Sahana B. Moodakare [c,***], Ravi Kumar [a,b,*]

[a] Laboratory for High Performance Ceramics, Department of Metallurgical and Materials Engineering, Indian Institute of Technology-Madras (IIT Madras), Chennai, 600036, India
[b] Ceramic Technologies Group-Center of Excellence in Materials and Manufacturing for Futuristic Mobility, Indian Institute of Technology-Madras (IIT Madras), Chennai, 600036, India
[c] Centre for Automotive Energy Materials, International Advanced Research Centre for Powder Metallurgy and New Materials, IITM Research Park, Taramani, Chennai, 600113, India
[d] Department of Chemistry, Institute of Inorganic Chemistry, University of Cologne, Greinstraße 6, 50939, Cologne, Germany

ARTICLE INFO

ABSTRACT

TiNb$_2$O$_7$/carbon nanocomposites synthesized through a simple, surfactant assisted precursor route is reported as a promising alternative anode material for lithium-ion batteries (LIBs). The carbon component of the nanocomposites is derived from an inexpensive and sustainable keratin rich biological source. The reinforcement of carbon in TiNb$_2$O$_7$ facilitated the formation of non-stoichiometric (Ti$_{0.712}$Nb$_{0.288}$)O$_2$ crystalline phase, in addition to the stoichiometric TiNb$_2$O$_7$ phase. It also yielded a high specific surface area (~90 m^2 g^{-1}) and reduced crystallite size (~4 nm). Electrochemical results exemplified high reversible capacity of 356 mAh g^{-1} at 0.1 C and remarkable rate capability of ~26 mAh g^{-1} at ultra-high current rate of 32C. TiNb$_2$O$_7$/carbon nanocomposites also demonstrated remarkable cyclic stability with large capacity retention of 85% even after 50 cycles at 1 C. The experimental data attests the potential of TiNb$_2$O$_7$/keratin derived carbon nanocomposites as economically and environmentally viable promising anode material for LIBs.

1. Introduction

The last two decades have witnessed rapid scientific inquisitiveness and technological development of lithium-ion batteries (LIBs) to address the soaring global energy demands [1,2]. In contrast to conventional rechargeable batteries, LIBs display high gravimetric and volumetric capacities [3–5]. This makes them potential candidates for portable electronics, miniaturized devices, and transportation applications [6]. However, to meet increased global energy demand, it is imperative to develop energy storage devices with amalgamation of high energy and power density along with robust cyclic stability and improved safety features. The performance of conventional lithium-ion technologies with graphite as anode material is limited by its low working potential (~0.1 V

vs. Li/Li$^+$) which leads to the formation of passivating solid-electrolyte interphase (SEI) resulting in poor cycle life and safety related issues [7]. The SEI in turn leads to the formation of lithium dendrites which on continuous growth penetrate the separator leading to possible short circuit and fire [8]. Moreover, the graphite-based anode chemistry requires a formation cycle prior to the application which directly impacts the cost and time of production line. Owing to the challenges posed by graphite anodes, exploring alternative anode materials with high energy storage capabilities is in order.

Recently, monoclinic TiNb$_2$O$_7$ (TNBO) was proposed as potential alternative anode material for LIB owing to its large theoretical capacity of 387 mAh g^{-1} and high working potential of ~1.6 V, preventing formation of SEI layers and lithium dendrites [9–15]. Albeit the aforementioned

Fig. 1. Ragone chart showing rate capabilities comparison of earlier works on different forms of $TiNb_2O_7$ materials: Nano-structured form of $TiNb_2O_7$ [nanoparticles [17], ordered macroporous [13], nanorods [18] and nanofibers [19]], Doped $TiNb_2O_7$ [$Mo_{0.05}Ti_{0.95}Nb_2O_7$ [20], $V_{0.02}TiNb_{1.98}O_7$ [21]] and $TiNb_2O_7$ carbon composites [CNT [10], graphene [22] and graphene oxide [23]].
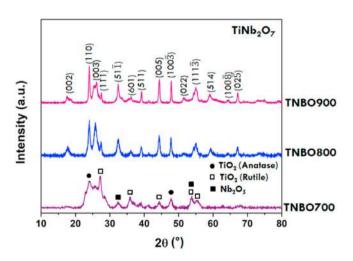

Fig. 2. X-ray diffractograms of pristine TNBO heat-treated at different temperatures.

Table 1
Specific surface area, pore size and pore volume of TNBO heat-treated at 700 °C, 800 °C and 900 °C.

Sl. No.	Sample	Pore size (nm)	Pore volume (cm^3 g^{-1})	BET surface area (m^2 g^{-1})
1.	TNBO700	8.0	0.22	108.0
2.	TNBO800	29.0	0.20	28.0
3.	TNBO900	51.0	0.10	9.0
4.	TNBO/ KC	6.0	0.13	89.0
5.	KC	7.0	0.0018	3.0

nano-structuring of TNBO is reported to facilitate the fast diffusion of lithium-ions between the electrode-electrolyte interface boosting electrochemical performance. In the case of doped TNBO and TNBO-carbon composites, dopants and carbon component, respectively contribute towards increase in ionic and electronic conductivity of TNBO. The comparison of rate capabilities of these materials is shown in the Ragone chart (Fig. 1). The superior performance of TNBO/carbon composites is imperative in contrast to doped TNBO and nano-structured forms of TNBO. Most of the earlier work reports fabrication of TNBO/carbon composites employed CNT, graphene and graphene oxide as carbon sources which beside being expensive also involve complex and specialized preparation routes limiting their scalability for possible use in LIBs.

Although presence of carbon in TNBO/carbon composites contribute towards performance enhancement of LIBs *via.* improved electrical and ionic conductivities, the role of nano-structuring on the improvement of the electrochemical performance and conversion efficiency cannot be derelict.

In this context, it is expected that a hybrid, nano-structured TNBO/ carbon composite as anode materials will synergistically combine good electrochemical interactions concomitant with improved electronic and ionic conductivities resulting in high performing LIBs. This study reports on the development of such a unique material system that uses inexpensive and sustainable keratin-derived biological carbon sources as reinforcement to fabricate porous nanocrystalline TNBO/carbon composites *via.* surfactant assisted precursor route. The electrochemical performance of these nanocomposites has been comprehensively evaluated and the potential of these materials for the development of anode materials for LIBs is explored.

2. Experimental section

2.1. Materials synthesis

2.1.1. Preparation of keratin derived carbon
Poultry feathers considered as waste biomass were washed with distilled water and oven dried at 100 °C for 24 h under ambient atmosphere. The dried feathers were further heat-treated at 225 °C for 10 h, and pyrolyzed at 800 °C for 3 h at a heating and cooling rate of 1 °C/min under N_2 atmosphere and the pyrolyzed product is referred to KC in the manuscript.

2.1.2. Synthesis of pristine TNBO
Pristine TNBO was synthesized through surfactant assisted precursor route following reported literature [24]. In the first step, pluronic F-127 (Mol. wt. ~12,600 g mol^{-1}, Sigma Aldrich, Bangalore, India) was added to a solution composed of C_2H_5OH, HCl and CH_3COOH, followed by vigorous stirring to attain a clear solution. Subsequently, $Ti(OC_3H_7)_4$ (97%, Sigma Aldrich, Bangalore, India) and $Nb(OC_2H_5)_5$ (99%, Sigma Aldrich, Bangalore, India) in the molar ratio of 1:2 was added dropwise and stirred for 1 h to yield TNBO suspension, followed by drying at 80 °C for 12 h. Thus, obtained powder was calcined at three different heat-treatment temperatures *viz.,* 700 °C, 800 °C and 900 °C for 3 h at a heating and cooling rate of 3 °C/min under ambient atmosphere and are designated as TNBO700, TNBO800 and TNBO900, respectively.

advantages, TNBO possess low electronic ($<10^{-9}$ S cm^{-1}) [16] and ionic conductivity. It also suffers from low Li-ion diffusion coefficient (D_{Li}) resulting in poor rate capability. The enhancement of the rate capability of TNBO has been explored through nano-structured forms of TNBO (particles, fibers, rods and porous), doped TNBO (Mo,V) and TNBO carbon composites [carbon nanotubes (CNT), graphene and graphene oxide] which are reported widely in literature [10,13,17–23]. The
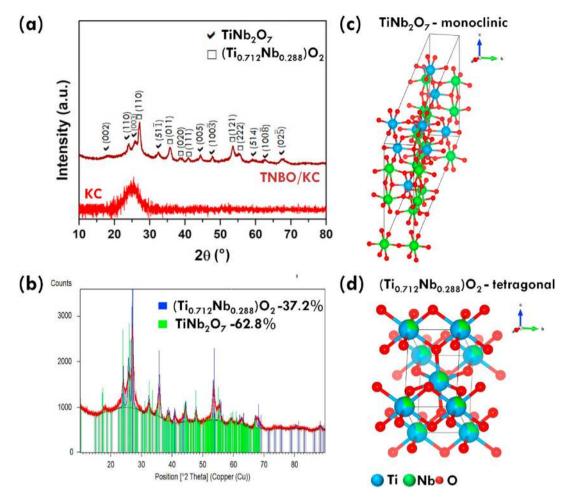
Fig. 3. (a) and (b) X-ray diffractograms of KC and TNBO/KC nanocomposites, respectively. (c) and (d) crystal structures of $TiNb_2O_7$ and $(Ti_{0.712}Nb_{0.288})O_2$, respectively.

2.1.3. Synthesis of TNBO/KC nanocomposites

TNBO/KC composites was prepared by adding KC to TNBO suspension (weight ratio of 50:50) following similar procedure as described in section 2.1.2 for complete volatilization of the solvent. The composite powder was subsequently heat-treated at 800 °C for 3 h at a heating and cooling rate of 3 °C/min under N_2 atmosphere.

2.2. Material characterization

The phase evolution of pristine TNBO and TNBO/KC nanocomposite was characterized by X-ray diffraction (XRD, Bruker AXS D8 Discover, USA) using Cu-K$_\alpha$ radiation (40 kV, 40 mA; step scan of 0.051, counting time of 5 s/step and 1.5460 Å). The crystallite size was calculated from the line broadening analysis of the most intense diffraction peak using Scherrer's equation; $D = K\lambda/(\beta\cos\theta)$, where D-coherently diffracting domain size (average crystallite size), K- shape factor (0.94), λ-wavelength of X-ray radiation, β-full width at half maximum (FWHM) measured in radians and θ-Bragg angle. The quantitative phase analysis and structural refinement of the diffracted pattern was performed through Rietveld analysis using HighScore Plus 3.0 software (Malvern PANalytical, The Netherlands). The Raman spectra (Labram HR 800, Horiba, Minami-Ku, Kyoto, Japan) was recorded using He–Ne laser source (488 nm) in the range of 100–4000 cm^{-1}. The weight percentage of KC in TNBO of TNBO/KC nanocomposite was evaluated using thermogravimetric analysis (TGA, TG instrument (NET ZSCH STA 409C). Brunauer–Emmett–Teller specific surface area (S$_{BET}$) and Barrette-Joynere-Halenda (BJH) pore size distributions were obtained from standard nitrogen adsorption-desorption isotherms measured by a surface area analyzer (TriStar 3020, Micromeritics, Norcross, GA, USA). Before measurements, the samples were degassed at 100 °C for 12 h under vacuum. The surface morphology was studied using high-resolution scanning electron microscopy (HRSEM, Apreo S, USA) and transmission electron microscopy (TEM, Tecnai T20), respectively. The SEM samples were gold sputtered prior to imaging and TEM samples were prepared by pulverizing the samples to fine sub-micrometer sized particles and dispersed in acetone to form a uniform dispersion, which was drop-casted on a carbon-film-coated copper grid. X-ray photoelectron spectroscopy (XPS) was carried out with an ESCA M-Probe (Al Kα rays, λ = 8.33 Å) in a detector range of 0–1000 eV. The detector pass energies were 158.28 eV for survey spectra and 55.22 eV for high-resolution (HR) spectra. Spectra of $TiNb_2O_7$ were referenced to 285 eV according to the adventitious carbon signal. For the $TiNb_2O_7$/KC sample, the spectra were referenced to 284.2 eV in line with a graphitic carbon signal and were fitted with an asymmetric LA(1,2,0) line shape [25]. For all spectra, a Shirley background, and besides the C=C peak, all other peaks were fitted with a GL(30) line shape using CasaXPS software from Casa Software Ltd.

2.3. Electrochemical tests

The electrochemical performance was accessed using CR2016-type coin cells fabricated in a dry argon-filled glove box. The anode materials were prepared by homogenous mixing of 80 wt % TNBO800 or TNBO/KC powders, 10 wt % polyvinylidene fluoride (PVDF) and 10 wt % conductive carbon (Super P®) in N-methylpyrrolidone (NMP). Thus, formed slurry was uniformly casted onto Cu foils and vacuum-dried at
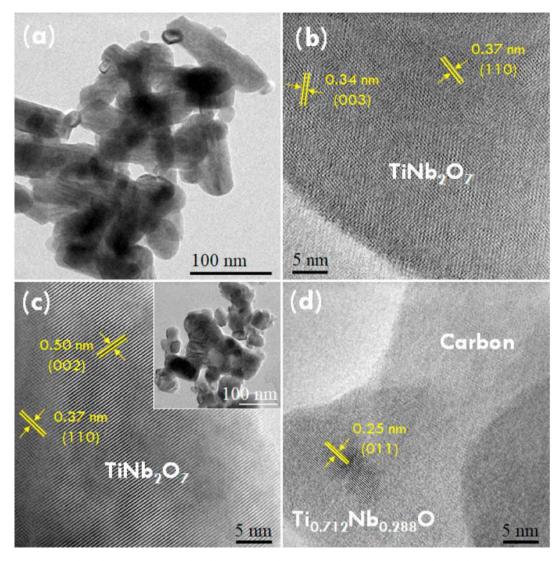
Fig. 4. (a) TEM image of TNBO, (b) and (c) HRTEM image of $TiNb_2O_7$ nanocrystals in TNBO and TNBO/KC, respectively and (d) HRTEM image of TNBO/KC showing reduced phase of $(Ti_{0.712}Nb_{0.288})O_2$ and carbon. The inset image in Fig. 4. (c) shows TEM image of TNBO/KC.
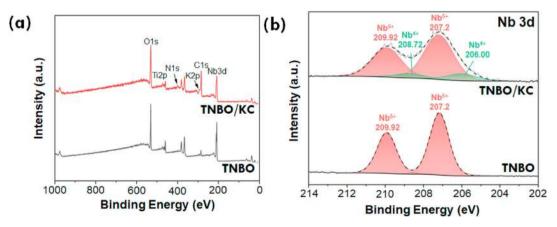

Fig. 5. (a) X-ray photoelectron survey spectra and (b) HR spectra Nb 3d of TNBO and TNBO/KC.

120 °C for 10 h. The cased Cu foils were roller-pressed to form the working electrodes with active material mass loading of ~4 mg cm^{-2}. Li foils were employed as both counter and reference electrodes. Microporous polypropylene films (Celgard 2325) acted as separators. The electrolyte was composed of 1 M solution of LiPF$_6$ (DAN VEC) in ethylene carbonate (EC)/dimethyl carbonate (DMC)/ethyl methyl carbonate (EMC) with a volume ratio of 1:1:1. The cells were designated as TNBO‖Li and TNBO/KC‖Li. Cyclic voltammetry (CV) experiments were conducted using an electrochemical workstation (Bio logic BCS810) at a scan rate of 0.05 mV s^{-1}. The galvanostatic charge-discharge tests were

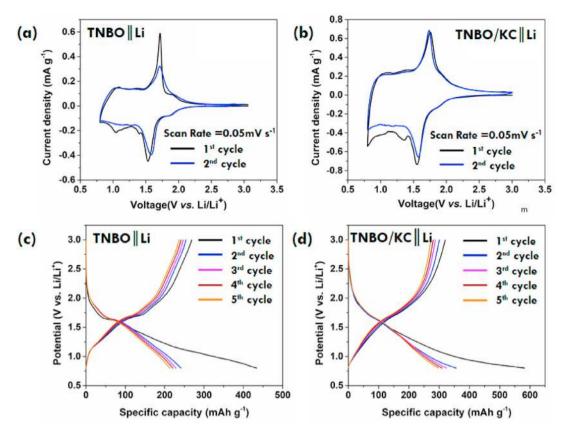**Fig. 6.** CV plots of (a) TNBO∥Li and (b) TNBO/KC∥Li cells, charge-discharge profiles of (c) TNBO∥Li and (d) TNBO/KC∥Li cells at 0.1 C (1 C = 387 mAh g^{-1}).
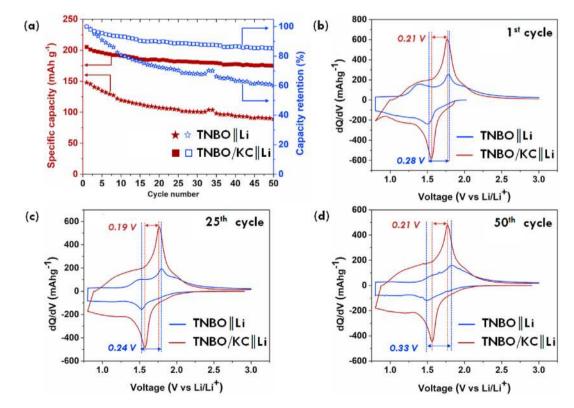

Fig. 7. (a) Cyclic stability of TNBO∥Li and TNBO/KC∥Li cells at 1C. dQ/dV curves of TNBO∥Li and TNBO/KC∥Li cells derived from 1 C rate at (b) 1st cycle, (c) 25th cycle and (d) 50th cycle.
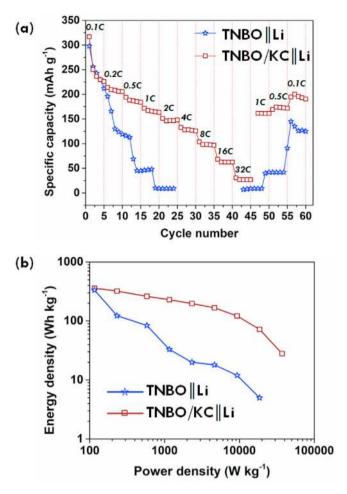
Fig. 8. (a) Rate capabilities of TNBO‖Li and TNBO/KC‖Li cells at different current rates and (b) Ragone plot of TNBO‖Li and TNBO/KC‖Li cells.

recorded at different current rates (0.1C–32 C) using a multi-channel battery testing system (Biologic) in a potential range of 3.0 V–0.8 V. The electrochemical impedance spectroscopy (EIS) was measured in a frequency range of 100 kHz to 0.01 Hz. The EIS spectra was recorded at open circuit voltage by applying a small amplitude of signal in an equilibrium state.

3. Results and discussion

3.1. Material characterization

Fig. 2 shows the X-ray diffractograms of TNBO powder heat-treated at various temperatures *viz.* 700 °C, 800 °C and 900 °C. At 700 °C, a broad peak was obtained matching with mixed phases of rutile and anatase of TiO_2 and monoclinic form of Nb_2O_5 phases indicating incomplete crystallization of $TiNb_2O_7$ at this temperature. On the contrary, at 800 °C and 900 °C the diffractograms were found to be matching with monoclinic $TiNb_2O_7$ crystallographic system [2θ = 24.1° (002), 23.9° (110), 25.9° (003), 32.4° (51$\bar{1}$), 44.0° (005) and 44.4° (100$\bar{3}$). No peaks corresponding to other forms of impure oxides were found, suggesting formation of phase-pure $TiNb_2O_7$ at a low temperature (800 °C).

The physical structural characteristics of $TiNb_2O_7$ were investigated through nitrogen adsorption-desorption isotherms to understand the surface area and porosity. Fig. S1 shows the corresponding BET isotherms exhibiting characteristic type IV adsorption-desorption behavior [Fig. S1 (a)] with a distinctive hysteresis loop in the relative pressure (p/p) ranging from 0.4 to 1. The pore size distribution curve [Fig. S1 (b)] exhibited mesoporous structure with distinct variation in pore size,

volume and BET surface area (Table 1). On increasing the heat-treatment temperature, increase in pore size and decrease in pore volume were observed, which is due to $TiNb_2O_7$ crystal growth resulting in disruption of primary mesoporosity. As a result, the BET surface area decreases from 108 m^2 g^{-1} to 9 m^2 g^{-1} on increasing the calcination temperature (Table 1). The X-ray diffractogram of TNBO700 revealed presence of mixed oxides, whereas the diffractogram of TNBO800 and TNBO900 displayed the presence of phase pure $TiNb_2O_7$ [Fig. 2]. However, TNBO900 exhibited lower surface area (9 m^2 g^{-1} *vs.* 28 m^2 g^{-1}) as compared to TNBO800. Hence, samples heat-treated at 800 °C was selected for all further studies.

Fig. S2 (a) shows TGA curve of calcined TNBO/KC nanocomposites. A single stage weight loss is observed around 400 °C to 650 °C with a weight loss of 47%, which is attributed to the oxidation of carbon in KC resulting in a ceramic yield of 53 wt % revealing weight ratio of KC:TNO (47:53) in TNBO/KC nanocomposites similar to weight ratio of KC:TNO (50:50) before heat-treatment. Further, the nature of carbon in KC and TNBO/KC nanocomposites was studied using Raman spectroscopy. Fig. S2 (b) displays the Raman spectra of pristine TNBO, KC and TNBO/ KC nanocomposites. Pristine TNBO shows three sharp peaks corresponding to edge shared TiO_6 octahedra (641 cm^{-1}) and corner shared NbO_6 octahedra (889 cm^{-1} and 1001 cm^{-1}). Both KC and TNBO/KC nanocomposites shows typical D and G peaks of carbon around 1330 and 1570 cm^{-1}, respectively. The relative intensity ratio of the D and G peaks (I_D/I_G) of KC is found to be 1.63, whereas in TNBO/KC nanocomposites the intensity ratio decreased to 1.20. This is due to increase in the degree of ordering or crystallinity in the free carbon in TNBO/KC nanocomposites as a result of the carbothermal reduction reaction between TNBO and KC. Moreover, TNBO/KC nanocomposites displays a broad peak at ~641 cm^{-1} indicating formation of smaller crystallite sized $TiNb_2O_7$. The broadening of the peak can also be attributed to the formation of non-stoichiometric phase due to oxygen vacancies [26].

Fig. 3 (a) shows the X-ray diffractograms of KC and TNBO/KC nanocomposites. The carbon derived from keratin at 800 °C demonstrates a broad peak around 2θ = ~25.2° indicating the amorphous nature of KC. Interestingly, TBNO/KC nanocomposites shows peaks corresponding to $TiNb_2O_7$ [monoclinic, C2/m (Fig. 3 (c)] phase along with new peaks corresponding to $(Ti_{0.712}Nb_{0.288})O_2$ [tetragonal, P 42/m, Figs. 3 (d), 2θ = 27.1° (110), 35.6° (011) and 53.7° (121)] phase, which were absent in pristine TNBO800 [Fig. 2]. The Rietveld refinement of TNBO/KC nanocomposites revealed 63% and 37% of $TiNb_2O_7$ and $(Ti_{0.712}Nb_{0.288})O_2$ phases, respectively [Fig. 3 (b)]. The formation of new peaks is attributed to the carbothermal reduction of TNBO with the carbon in TNBO/KC, resulting in reduced non-stoichiometric oxide phase having shared lattice sites of Ti and Nb atoms in the crystal structure of $(Ti_{0.712}Nb_{0.288})O_2$ [Fig. 3 (d)] concordant with Raman results. The O^{2-} vacancies in the crystal structure of non-stoichiometric $(Ti_{0.712}Nb_{0.288})O_2$ phase imparts electrical conductivity due to electronic disorder. Similar observations were also made by Chunfu Lin *et. al.,* [10] where $TiNb_2O_7$/carbon nanotubes composite showed formation of reduced non-stoichiometric oxide, $Ti_2Nb_{10}O_{29}$ phase due to carbothermal reduction of $TiNb_2O_7$ with carbon nanotubes. Moreover, the XRD of both TNBO800 [Fig. 2] and TNBO/KC [Fig. 3 (a)] showed broad peaks, indicating the formation of smaller grain sized crystals. The average crystallite sizes of $TiNb_2O_7$ in TNBO800 and $TiNb_2O_7$ and $(Ti_{0.712}Nb_{0.288})O_2$ phases in TNBO/KC were calculated using Scherrer equation. In the case of pristine TNBO800, the average crystallite size of $TiNb_2O_7$ was determined to be ~13 nm, whereas in TNBO/KC nanocomposites displayed crystallite size of ~4 nm and ~11 nm for $TiNb_2O_7$ and $(Ti_{0.712}Nb_{0.288})O_2$, respectively. The smaller crystallite size in TNBO/KC nanocomposites can be ascribed to the existence of KC, leading to the formation of CO and CO_2 gases during precursor to ceramic conversion process hindering $TiNb_2O_7$ crystallite growth. This is further corroborated from the results of BET, SEM and TEM.

Fig. S3 (a) and (b) presents the BET isotherms and pore size distribution, respectively of KC and TNBO/KC nanocomposites. The pore size

Table 2
Performance comparison of electrochemical data of pristine TNBO and TNBO/KC nanocomposites with previously reported graphite, TiO_2 and Nb_2O_5 based electrode materials.

Anode materials	Voltage Range [V vs Li/Li$^+$]	Electrolytes	Columbic efficiency after X number of cycles and specific capacity, mAh g^{-1} [C-rate]	Specific capacity, mAh g^{-1} at different C-rate	Ref
Graphite (pristine)	0.005 to 2	1.0 M LiPF$_6$ EC/DMC/EMC (1:1:1; V/V/V)	NA	334(C/10), 215 (1C), 89 (2C), 33 (5C), 18 (10C), 11 (20C), 7 (40C)	[34]
Graphite (carbon coated)	0.01 to 1	1.0 M LiPF$_6$ in PC:DMC (1:1; V/V)	98% after 60 cycle; 350 [C/5]	375(C/20), 350(C/2), 345 (1C), 275 (2C), 220 (3C), 50 (10C)	[35]
Graphite (AlF$_3$ coated)	0.01 to 1.2	1.0 M LiPF$_6$ in EC–EMC (3:7; V/V)	91% after 300 cycle; 300 [C/5]	345(C/20), 335(C/10), 250(C/5), 150 (1C), 50 (2C), 25 (5C)	[36]
Graphite (pristine)	0.005 to 1.5	1.2 MLiPF$_6$ in EC/EMC (1:1 V/V) + 2 wt% VC	NA	360(C/10), 320 (3C), 234 (5C), 100 (10C)	[37]
Graphite (pristine)	0.01 to 3.0	1.0 M LiPF$_6$ in EC/DMC (1:1 V/V)	99.5% after 100 cycles; 360 [C/5]	360(C/5), 350 (1C), 320 (2C), 210 (3C), 130 (4C), 100 (5C), 90 (6C)	[38]
TiO$_2$	1.0 to 3.5	1.0 M LiPF$_6$ in EC/DMC (1:1, V/V)	99% after 20 cycle; 175 [C/20]	170(C/20), 168(C/10), 162(C/5), 160(C/2), 130 (1C), 100 (2C)	[39]
Graphene/TiO$_2$ nanocomposites	1.0 to 3.0	1 M LiPF$_6$ in EC/DMC (1:1, V/V)	98% after 50 cycle; 175 [C/5]	170(C/5), 160 (1C), 140 (3C), 120 (5C), 110 (10C)	[40]
TiO$_2$ (nanotube)	1.1 to 3.0	1.0 M LiPF$_6$ in EC/DMC (1:1; w/w)	99% after 300 cycles; 145 [C/10]	175(C/20), 155(C/10), 85 (10C)	[41]
TiO$_2$ (N-doped)	1.0 to 2.5	1.0 M LiPF$_6$ EC/DMC (1:1; V/V)	99% after 100 cycles; 200 [C/2]	250(C/10), 225(C/2), 200 (1C), 180 (2C), 150 (5C), 125 (10C)	[42]
Nb$_2$O$_5$ (nanosheet)	1.0 to 2.5	1 M LiPF$_6$ in EC/DMC/DEC (1:1:1; V/V/V)	99.8% after 100 cycles; 117 [C/5]	165 (1C), 135 (2C), 70 (5C)	[43]
Nb$_2$O$_5$ (3D urchin-like microstructure)	1 to 3.0	1.0 M LiPF$_6$ in EC/DMC (1:1; V/V)	99.8% after 1000 cycles; 130 [1C(1A/g)]	175(C/5), 165(C/2), 150 (1C), 120 (2C), 85 (5C)	[44]
TNBO	0.8 to 3.0	1.0 M LiPF$_6$ in EC/DMC/EMC (1:1:1; V/V/V)	66.2% after 50 cycles; 269 [C/10]	296(C/10), 118(C/5), 44 (1C), 9 (2C)	This work
TNBO/KC	0.8 to 3.0	1.0 M LiPF$_6$ in EC/DMC/EMC (1:1:1; V/V/V)	99.8% after 50 cycles; 356 [C/10]	320(C/10), 195(C/5), 175 (1C), 153 (2C), 132 (4C), 103 (8C), 63 (16C), 26 (32C)	This work

● TiNb$_2$O$_7$ nanocrystals
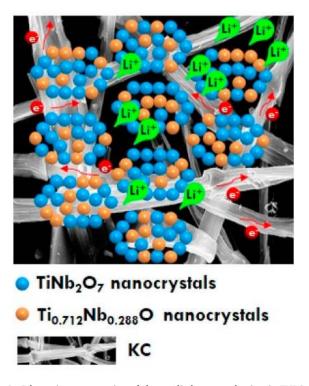
● Ti$_{0.712}$Nb$_{0.288}$O nanocrystals

▬ KC

Fig. 9. Schematic representation of charge/discharge mechanism in TNBO/KC nanocomposites.

distribution curve demonstrated the presence of mesopores in TNBO/KC composite, whereas KC is comprised of macroporous [Fig. S3 (a)].

Moreover, KC exhibits average pore size of ~7.0 nm and very low S_{BET} of 3.0 m^2 g^{-1}. The low surface area is possibly due to retention of fibrilous structure under careful carbonization, which is evidenced in SEM micrograph as well [insert image of Fig. S4 (b)]. Interestingly, the addition of KC resulted in drastic reduction of the average pore size of TNBO/KC nanocomposites ~6.0 nm and increase in S_{BET} to 89.0 m^2 g^{-1} in comparison to pristine TNBO800 (29.0 nm and 28.0 m^2 g^{-1}), which is higher than the so far reported works on TNBO/carbon composites.

The morphology of pristine TNBO800, KC and TNBO/KC nano-composites was investigated using HRSEM and HRTEM analyses (Fig. S4 and Fig. 4). It was observed that KC remarkably retained the fibrilous structure post carbonization process yielding carbon microtubes with an average diameter of ~26.0 μm and thickness of ~2.0 μm [insert image of Fig. S4 (b)]. In both the cases pristine TNBO800 and TNBO/KC, nano-crystals with interconnected porous scaffold like structure with distinct variation in crystallite size was observed [Fig. S4 (a) and Fig. S4 (c)]. The average crystallite size of pristine TNBO800 was determined to be ~78.0 nm, whereas in TNBO/KC, a drastic reduction of crystallite size to ~35.0 nm was observed. Moreover, carbon microtube structure observed in KC is not retained in TNBO/KC nanocomposites [Fig. S4 (c)], which is possibly due to carbothermal reduction reaction of KC with TNBO resulting in destruction of fibrilous structure.

HRTEM micrographs of TNBO and TNBO/KC nanocomposites are exemplified in Fig. 4. The TEM micrograph of TNBO [Fig. 4 (a)] exhibited agglomerated TiNb$_2$O$_7$ nanocrystals. Furthermore, the lattice fringes in the HRTEM image [Fig. 4 (b)] shows lattice spacing of 0.37 nm and 0.34 nm corresponding to the diffraction planes of TiNb$_2$O$_7$ nanocrystals (110) and (003) respectively corroborating with the XRD results. The TEM micrograph of TNBO/KC composite revealed uniformly dispersed TiNb$_2$O$_7$ nanocrystals in KC matrix indicating better anchorage with incorporation of KC [insert image of Fig. 4 (c)]. A strong lattice fringe with a lattice spacing of 0.25 nm matches perfectly with (011) planes of (Ti$_{0.712}$Nb$_{0.288}$)O$_2$ [Fig. 4 (d)] in line with XRD results (Fig. 3).

X-ray photoelectron spectroscopy (XPS) was further employed to analyze the chemical environment of Ti, Nb, C, and O elements in TNBO and TNBO/KC. Survey scans of both samples reveal the existence of Ti, Nb, C, and O as expected [Fig. 5 (a)]. Besides these signals, N and K were also observed, which belong to contaminations of the pyrolysis processes.

The presence of carbon (18.46 at.%) in TNBO can be attributed to adventitious carbon. In TNBO/KC the higher amount of carbon (58.44 at.%) appertains to the added carbon source. High-resolution investigations showed the presence of C=C (sp^2, 284.2 eV) bonds for the TNBO/KC and C–C (sp^3, 285 eV) bonds for the pristine, which can be easily seen in the peak shift (dotted lines, $\Delta 0.8$ eV) and the asymmetric line shape in Fig. S5 (b) [25]. Moreover, for the pristine sample signals of hydroxyl, carbonyl, and carboxyl groups at binding energies of 286.5, 288.0, and 289.0 eV were detected, whereas for the sample with TNBO/KC besides the C=C peak a characteristic pi-pi* transition shake-up at 291 eV and a carboxyl peak at 289 eV was observed [25,27].

As expected, high-resolution analysis of Nb 3d peak displays a doublet peak with an area ratio of 2:3 for Nb 3d 5/2 and Nb 3d 3/2, respectively. The binding energy of 207.2 eV for the Nb 3d 5/2 and a spin-orbit-splitting of $\Delta 2.72$ eV correspond to the pure pentavalent Nb in TiNb$_2$O$_7$ [Fig. 5 (b)] [28,29]. In addition, HR spectra of Ti 2p pointed out that titanium is in the valance state +4 (Ti 2p 3/2: 458.61 eV, Ti 2p 1/2: 464.26 eV) [Fig. S5 (a)] [30]. In comparison to the TNBO/KC sample, titanium was also detected in the valance state 4+, whereas the HR spectra of Nb 3d displays beside the pentavalent Nb (207.2 eV) also the tetravalent Nb (206.0 eV) [Fig. 5 (b)] [28]. This is in good agreement with the XRD measurements, that after the carbothermal reduction niobium is present in valance states 4+ (Ti$_{0.712}$Nb$_{0.288}$O$_2$) and 5+ (TiNb$_2$O$_7$).

The main peak of the O 1s orbital was fitted to the metal-oxygen bonds (Ti–O, Nb–O) centered at 530.2 eV while hydroxides and carbon oxides were fitted at 531.3 and 532.5 eV [29]. As already seen in the HR C 1s spectrum only a small amount of oxygen is bonded to carbon which is evident in the O 1s high-resolution spectra of TNBO/KC [Fig. S5 (c)].

3.2. Electrochemical performance evaluation

The surface-active electrochemical phenomenon for TNBO∥Li and TNBO/KC∥Li cells were studied using cyclic voltammetry (CV). The CV experiments were conducted in half-cell configuration with respect to Li metal in the voltage range 0.8–3.0 V at the scan rate of 0.05 mV s^{-1} for 2 cycles. The corresponding voltammograms are presented in Fig. 6 (a) and (b).

The single pair of prominent cathodic/anodic peaks at 1.50 V/1.67 V and 1.56 V/1.74 V for TNBO∥Li and TNBO/KC∥Li cells, respectively are attributed to the redox couple of Nb^{5+}/Nb^{4+}. The shoulder peak at 1.80 V and 1.90 V in TNBO∥Li and TNBO/KC∥Li cells, respectively is ascribed to Ti^{4+}/Ti^{3+} redox couples. The peaks at low voltage of 1.24 V and 1.33 V in TNBO∥Li and TNBO/KC∥Li cells, respectively is assigned to Nb^{4+}/Nb^{3+} redox couples. Nevertheless, TNBO/KC∥Li cell displayed symmetric redox couple and larger peak intensities revealing good reversable cycling process and better electrochemical kinetics as compared to TNBO∥Li cell.

The galvanostatic charge-discharge tests of the TNBO∥Li and TNBO/KC∥Li cells were conducted at different current rates (theoretical capacity at 1 C = 387 mAh g^{-1}) in the voltage range of 0.8–3.0 V. Fig. 6 (c) and (d) shows charge-discharge profile of TNBO∥Li and TNBO/KC∥Li cells, respectively for the first five cycles at 0.1 C rate. It is noteworthy that, the 1st cycle of both TNBO∥Li and TNBO/KC∥Li cells exhibited very high initial discharge capacity of 434 mAh g^{-1} and 582 mAh g^{-1} and low initial columbic efficiency of 62.0% and 55.0%, respectively. This is ascribed to the degradation of the electrolyte and SEI formation [22]. Furthermore, keratin derived carbon possesses more active intercalation sites as demonstrated by the prevalence of D-band in Raman spectra [Fig. S2 (b)]. This indicates the existence of C=O, C–O, and O–C=O functional groups as well as nitrogen dopants which are reported to

contribute in lithium intercalation leading to high initial discharge capacity [31] and low initial columbic efficiency in TNBO/KC∥Li as compared to TNBO∥Li. In the 2nd cycle, TNBO/KC∥Li demonstrated high discharge capacity of 356 mAh g^{-1} in comparison to 269 mAh g^{-1} for TNBO∥Li. It is noteworthy that, the reversible capacities obtained in TNBO/KC∥Li cell is much higher than so far reported work in TiNb$_2$O$_7$ nanocomposites and twice the value of Li$_4$Ti$_5$O$_{12}$ (~170 mAh g^{-1}) [32] indicating its practical applicability as anode material in LIBs. Moreover, TNBO/KC∥Li cell retained higher reversible capacity of 175 mAh g^{-1} after 50 cycles when cycled at 1 C rate along with a high-capacity retention of 85% and columbic efficiency of ~99% (Fig. S6). On the contrary, TNBO∥Li cell showed poor performance with reversible capacity of 89 mAh g^{-1} after 50 cycles, with a low-capacity retention of 60% [Fig. 7 (a)] and columbic efficiency of ~66% (Fig. S6).

To understand the electrochemical process involved in charge/discharge cycles at 1 C rate, dQ/dV plots were derived for 1st, 25th and 50th cycle [Fig. 7 (b), (c) and (d)]. In all the cases, the single pair of sharp peaks in discharge/charge process around 1.50 V/1.78 V and 1.55 V/1.76 V corresponds to the reduction/oxidation process of Nb^{5+}/Nb^{4+} in TNBO∥Li and TNBO/KC∥Li cells, respectively. The small peaks at low voltage of ~1.20 V and ~1.37 V in TNBO∥Li ascribes to Nb^{4+}/Nb^{3+} redox couples, however, these peaks are not noticeable in TNBO/KC∥Li. This may be due to existence of broader peaks as compared to TNBO∥Li. Moreover, on increasing the number of cycles, significant shift in redox peak position is observed in both TNBO∥Li and TNBO/KC∥Li cells. The difference in ΔV of the redox peaks is ascribed to over-potential at each step [33]. The ΔV values of TNBO∥Li are 0.28, 0.24, 0.33 V for 1st, 25th and 50th cycle, respectively, whereas TNBO/KC∥Li exhibited ΔV values of 0.21, 0.19, 0.21 V for 1st, 2^{5th} and 50th cycle, respectively. It is evidenced that TNBO/KC∥Li maintained low ΔV with smaller differences between the cycles as compared to TNBO∥Li. The better performance of TNBO/KC∥Li cell is attributed to the presence of highly anchored TNBO nanocrystals on the KC along with presence of homogeneously distributed composite which significantly improves the electric conductivity of TNBO in TNBO/KC nanocomposites. Fig. 8 (a) exhibits the rate capability studies of TNBO∥Li and TNBO/KC∥Li at different current rates ranging from 0.1 C to 32 C. At all C rates TNBO/KC∥Li showed higher cycling rates as compared to TNBO∥Li. It is very interesting to note that even at 8 C rate, TNBO/KC∥Li displayed a capacity of ~98 mAh g^{-1} whereas TNBO∥Li cell reached ~9 mAh g^{-1} at 2 C rate, indicating higher rate capability of TNBO/KC∥Li. On further increase in the cycling rates to 16 C and 32 C, TNBO/KC∥Li demonstrated a capacity of ~63 mAh g^{-1} and ~26 mAh g^{-1}, respectively, whereas TNBO∥Li displayed negligible capacity at these higher cycling rates. Fig. 8 (b) shows the Ragone plot, where TNBO/KC∥Li shows superior performance in terms of both energy and power density in comparison to TNBO∥Li. The electrochemical performance comparison data of TNBO and TNBO/KC nanocomposites with reported graphite, TiO$_2$ and Nb$_2$O$_5$ based electrode materials are given in Table 2. TNBO/KC exhibited higher rate capabilities as compared to the reported graphite, TiO$_2$ and Nb$_2$O$_5$ based electrode materials indicating its practical applicability as anode material for LIBs.

The lithium diffusion kinetics of TNBO∥Li and TNBO/KC∥Li was investigated through EIS studies. Fig. S7 (a) show the Nyquist plots of TNBO∥Li and TNBO/KC∥Li cells along with fitting curves and equivalent electrical circuit model. The Nyquist spectrum comprises of a sand a steep slope line in the high and low frequency region, respectively. The semicircle ascribes to the charge transfer resistance of Li-ion at interfacial region. As shown by the Nyquist plots, TNBO/KC∥Li exhibited smaller charge-transfer resistance (122 Ω *vs.* 223 Ω) as compared to TNBO∥Li revealing faster Li-ion transfer at the surface of the TNBO/KC nanocomposites electrode. The steep slope line is accredited to Warburg diffusion corresponding to the Li-ion diffusion into the structure of the active electrode materials. The D$_{Li}$ of TNBO∥Li and TNBO/KC∥Li can be determined using equations (1) and (2) [45,46],

$$Z' = R_1 + R_2 + \sigma\omega^{-1/2} \tag{1}$$

$$D_{Li} = \frac{R^2 T^2}{2A^2 n^2 F^4 C^2 \sigma^2} \qquad (2)$$

where Z' is the real part impedance, R_1 is the Ohmic resistance, R_2 is the charge-transfer resistance, ω is the angular frequency, σ is the Warburg factor calculated from the slope of plot between real part resistance *vs* inverse square root of angular frequency [Fig. S7 (b)], R is the gas constant, T is the temperature in K, A is surface area of the active materials measured from BET measurements, F is the faraday constant and C is the molar concentration of Li-ion in the active materials. From the fitting linear equation in Fig. S7 (b), the D_{Li} was determined to be 1.36×10^{-13} cm^2 s^{-1} and 2.63×10^{-13} cm^2 s^{-1} for TNBO‖Li and TNBO/KC‖Li, respectively indicating faster rate of Li-ion adsorption and insertion at $TiNb_2O_7$ nanoparticle surfaces in TNBO/KC nanocomposites.

3.2.1. Role of porous microstructure and reduced $(Ti_{0.712}Nb_{0.288})O_2$ phase in TNBO/KC nanocomposites

The remarkable electrochemical performance of TNBO/KC‖Li is ascribed to the unique structure of the nanocomposites as shown in the schematic (Fig. 9). The interconnected porous scaffold-like structure of $TiNb_2O_7$ and $(Ti_{0.712}Nb_{0.288})O_2$ nanocrystals in TNBO/KC [Fig. S4 (c) can effectively relieve the unexpected stress arising from continuous charge/discharging process of Li-ions, thereby facilitating the diffusion of Li-ions between the electrode-electrolyte interface. Whereas, the formation of reduced non-stoichiometric oxide phase having shared lattice sites of Ti and Nb atoms in the crystal structure of $(Ti_{0.712}Nb_{0.288})O_2$ [Fig. 3 (d) creates O^{2-} vacancies in the crystal structure imparting electrical conductivity due to electronic disorder. As a result, reduced $(Ti_{0.712}Nb_{0.288})O_2$ nanocrystals can act as conducting bridge to build a good electrical contact between $TiNb_2O_7$ nano crystallites and the carbon matrix which synergistically combines good electrochemical interaction with improved electronic and ionic conductivity leading to enhanced electrical conductivity, higher D_{Li} and lower charge-transfer resistance in contrast to pristine TNBO.

4. Conclusions

Porous and conductive TNBO/KC nanocomposites anode material for LIBs were synthesized from surfactant assisted precursor route followed by heat-treatment under N_2 atmosphere. Compared to pristine TNBO800, TNBO/KC yielded reduced crystalline $(Ti_{0.712}Nb_{0.288})O_2$ phase and $TiNb_2O_7$ phase with higher specific surface area (28 m^2 g^{-1} *vs.* 89 m^2 g^{-1}). TEM images discerned the presence of good contact between the $TiNb_2O_7$ nano crystallites and the carbon matrix. This aided in the reduction of crystallite size and enhancement of electrical conduction. Such synergistic effect resulted in better electrochemical performances of TNBO/KC as compared to pristine TNBO800. At 0.1 C, TNBO/KC showed high initial discharge capacity of 356 mAh g^{-1} in comparison to 269 mAh g^{-1} for TNBO800. Moreover, TNBO/KC retained higher reversible capacity at 1 C rate (175 mAh g^{-1} *vs.* 89 mAh g^{-1} over 50 cycles) along with higher capacity retention (85% *vs.* 60%) as compared to pristine TNBO800. At ultra-higher C rate of 32 C, TNBO/KC demonstrated remarkable stability with capacity of ~26 mAh g^{-1}. While, a capacity of only 9 mAh g^{-1} was obtained pristine for TNBO800 at 2 C. This exemplifies the potential of TNBO/KC nanocomposites as promising, economical, and environment friendly alternative anode materials for the commercialization of LIBs technology.

Funding sources

Appendix A. Supplementary data

Supplementary data to this article can be found online at https://doi.org/10.1016/j.oceram.2021.100131.

References

[1] M.A. Hannan, M.H. Lipu, A. Hussain, A. Mohamed, A review of lithium-ion battery state of charge estimation and management system in electric vehicle applications: challenges and recommendations, Renew. Sustain. Energy Rev. 78 (2017) 834–854.
[2] R. von Hagen, A. Lepcha, X. Song, W. Tyrra, S. Mathur, Influence of electrode design on the electrochemical performance of Li3V2 (PO4) 3/C nanocomposite cathode in lithium ion batteries, Nanomater. Energy 2 (2) (2013) 304–313.
[3] H.C. Hesse, M. Schimpe, D. Kucevic, A. Jossen, Lithium-ion battery storage for the grid—a review of stationary battery storage system design tailored for applications in modern power grids, Energies 10 (12) (2017) 2107.
[4] Y.L. Cheah, R. von Hagen, V. Aravindan, R. Fiz, S. Mathur, S. Madhavi, High-rate and elevated temperature performance of electrospun V2O5 nanofibers carbon-coated by plasma enhanced chemical vapour deposition, Nanomater. Energy 2 (1) (2013) 57–64.
[5] R. Von Hagen, H. Lorrmann, K.C. Möller, S. Mathur, Electrospun LiFe1− yMnyPO4/C nanofiber composites as self-supporting cathodes in Li-ion batteries, Adv. Eng. Mater. 2 (5) (2012) 553–559.
[6] P. Li, G. Zhao, X. Zheng, X. Xu, C. Yao, W. Sun, S.X. Dou, Recent progress on silicon-based anode materials for practical lithium-ion battery applications, Energy Storage Materials 15 (2018) 422–446.
[7] X. Han, L. Lu, Y. Zheng, X. Feng, Z. Li, J. Li, M. Ouyang, A review on the key issues of the lithium ion battery degradation among the whole life cycle, ETransportation 1 (2019) 100005.
[8] Q. Liu, C. Du, B. Shen, P. Zuo, X. Cheng, Y. Ma, G. Yin, Y. Gao, Understanding undesirable anode lithium plating issues in lithium-ion batteries, RSC Adv. 6 (91) (2016) 88683–88700.
[9] R. Inada, T. Mori, R. Kumasaka, R. Ito, T. Tojo, Y. Sakurai, Characterization of vacuum-annealed TiNb2O7 as high potential anode material for lithium-ion battery, Int. J. Appl. Ceram. Technol. 16 (1) (2019) 264–272.
[10] C. Lin, L. Hu, C. Cheng, K. Sun, X. Guo, Q. Shao, J. Li, N. Wang, Z. Guo, Nano-TiNb2O7/carbon nanotubes composite anode for enhanced lithium-ion storage, Electrochim. Acta 260 (2018) 65–72.
[11] G. Liu, L. Zhao, R. Sun, W. Chen, M. Hu, M. Liu, X. Duan, T. Zhang, Mesoporous TiNb2O7 microspheres as high performance anode materials for lithium-ion batteries with high-rate capability and long cycle-life, Electrochim. Acta 259 (2018) 20–27.
[12] M. Liu, H. Dong, S. Zhang, X. Chen, Y. Sun, S. Gao, J. Xu, X. Wu, A. Yuan, W. Lu, Three-Dimensional porous TiNb2O7/CNT-KB composite microspheres as lithium-ion battery anode material, ChemElectroChem 6 (15) (2019) 3959–3965.
[13] S. Lou, X. Cheng, Y. Zhao, A. Lushington, J. Gao, Q. Li, P. Zuo, B. Wang, Y. Gao, Y. Ma, Superior performance of ordered macroporous TiNb2O7 anodes for lithium ion batteries: understanding from the structural and pseudocapacitive insights on achieving high rate capability, Nanomater. Energy 34 (2017) 15–25.
[14] H. Yu, H. Lan, L. Yan, S. Qian, X. Cheng, H. Zhu, N. Long, M. Shui, J. Shu, TiNb2O7 hollow nanofiber anode with superior electrochemical performance in rechargeable lithium ion batteries, Nanomater. Energy 38 (2017) 109–117.
[15] G. Zhu, Q. Li, Y. Zhao, R. Che, Nanoporous TiNb2O7/C composite microspheres with three-dimensional conductive network for long-cycle-life and high-rate-

capability anode materials for lithium-ion batteries, ACS Appl. Mater. Interfaces 9 (47) (2017) 41258–41264.

[16] K.J. Griffith, I.D. Seymour, M.A. Hope, M.M. Butala, L.K. Lamontagne, M.B. Preefer, C.P. Koçer, G. Henkelman, A.J. Morris, M.J. Cliffe, Ionic and electronic conduction in TiNb2O7, J. Am. Chem. Soc. 141 (42) (2019) 16706–16725.

[17] L. Fei, Y. Xu, X. Wu, Y. Li, P. Xie, S. Deng, S. Smirnov, H. Luo, SBA-15 confined synthesis of TiNb 2 O 7 nanoparticles for lithium-ion batteries, Nanoscale 5 (22) (2013) 11102–11107.

[18] S. Lou, Y. Ma, X. Cheng, J. Gao, Y. Gao, P. Zuo, C. Du, G. Yin, Facile synthesis of nanostructured TiNb 2 O 7 anode materials with superior performance for high-rate lithium ion batteries, Chem. Commun. 51 (97) (2015) 17293–17296.

[19] K. Tang, X. Mu, P.A. van Aken, Y. Yu, J. Maier, "Nano-pearl-string" TiNb2O7 as anodes for rechargeable lithium batteries, Adv. Eng. Mater. 3 (1) (2013) 49–53.

[20] H. Song, Y.-T. Kim, A Mo-doped TiNb 2 O 7 anode for lithium-ion batteries with high rate capability due to charge redistribution, Chem. Commun. 51 (48) (2015) 9849–9852.

[21] X. Wen, C. Ma, C. Du, J. Liu, X. Zhang, D. Qu, Z. Tang, Enhanced electrochemical properties of vanadium-doped titanium niobate as a new anode material for lithium-ion batteries, Electrochim. Acta 186 (2015) 58–63.

[22] S. Li, X. Cao, C.N. Schmidt, Q. Xu, E. Uchaker, Y. Pei, G. Cao, TiNb 2 O 7/graphene composites as high-rate anode materials for lithium/sodium ion batteries, J. Mater. Chem. 4 (11) (2016) 4242–4251.

[23] A. Ashish, P. Arunkumar, B. Babu, P. Manikandan, S. Sarang, M. Shaijumon, TiNb2O7/Graphene hybrid material as high performance anode for lithium-ion batteries, Electrochim. Acta 176 (2015) 285–292.

[24] J. Fan, S.W. Boettcher, G.D. Stucky, Nanoparticle assembly of ordered multicomponent mesostructured metal oxides via a versatile sol– gel process, Chem. Mater. 18 (26) (2006) 6391–6396.

[25] T.L. Barr, S. Seal, Nature of the use of adventitious carbon as a binding energy standard, J. Vac. Sci. Technol.: Vacuum, Surfaces, and Films 13 (3) (1995) 1239–1246.

[26] A. Bharti, S. Muliankeezhu, G. Cheruvally, Pt–TiO2 nanocomposites as catalysts for proton exchange membrane fuel cell: prominent effects of synthesis medium pH, J. Nanosci. Nanotechnol. 18 (4) (2018) 2781–2789.

[27] G. Greczynski, L. Hultman, X-ray photoelectron spectroscopy: towards reliable binding energy referencing, Prog. Mater. Sci. 107 (2020) 100591.

[28] M. Bahl, ESCA studies of some niobium compounds, J. Phys. Chem. Solid. 36 (6) (1975) 485–491.

[29] M.A. Gomes, L.O.d.S. Bulhões, S.C. De Castro, A.J. Damião, The electrochromic process at Nb2 O 5 electrodes prepared by thermal oxidation of niobium, J. Electrochem. Soc. 137 (10) (1990) 3067.

[30] M.C. Biesinger, L.W. Lau, A.R. Gerson, R.S.C. Smart, Resolving surface chemical states in XPS analysis of first row transition metals, oxides and hydroxides: Sc, Ti, V, Cu and Zn, Appl. Surf. Sci. 257 (3) (2010) 887–898.

[31] S. Klink, E. Ventosa, W. Xia, F. La Mantia, M. Muhler, W. Schuhmann, Tailoring of CNT surface oxygen groups by gas-phase oxidation and its implications for lithium ion batteries, Electrochem. Commun. 15 (1) (2012) 10–13.

[32] J. Wang, H. Zhao, Y. Wen, J. Xie, Q. Xia, T. Zhang, Z. Zeng, X. Du, High performance Li4Ti5O12 material as anode for lithium-ion batteries, Electrochim. Acta 113 (2013) 679–685.

[33] H. Kim, Y. Lee, D. Byun, W. Choi, TiNb2O7 microsphere anchored by polydopamine-modified graphene oxide as a superior anode material in lithium-ion batteries, Int. J. Energy Res. 44 (6) (2020) 4986–4996.

[34] S.R. Sivakkumar, J. Nerkar, A. Pandolfo, Rate capability of graphite materials as negative electrodes in lithium-ion capacitors, Electrochim. Acta 55 (9) (2010) 3330–3335.

[35] V. Sharova, A. Moretti, G.A. Giffin, D.V. Carvalho, S. Passerini, Evaluation of carbon-coated graphite as a negative electrode material for Li-ion batteries, C—Journal of Carbon Research 3 (3) (2017) 22.

[36] F. Ding, W. Xu, D. Choi, W. Wang, X. Li, M.H. Engelhard, X. Chen, Z. Yang, J.-G. Zhang, Enhanced performance of graphite anode materials by AlF 3 coating for lithium-ion batteries, J. Mater. Chem. 22 (25) (2012) 12745–12751.

[37] U. Farooq, C.-H. Doh, S.A. Pervez, D.-H. Kim, S.-H. Lee, M. Saleem, S.-J. Sim, J.-H. Choi, Rate-capability response of graphite anode materials in advanced energy storage systems: a structural comparison, Carbon letters 17 (1) (2016) 39–44.

[38] H. Buqa, D. Goers, M. Holzapfel, M.E. Spahr, P. Novák, High rate capability of graphite negative electrodes for lithium-ion batteries, J. Electrochem. Soc. 152 (2) (2005) A474.

[39] M.-C. Yang, Y.-Y. Lee, B. Xu, K. Powers, Y.S. Meng, TiO2 flakes as anode materials for Li-ion-batteries, J. Power Sources 207 (2012) 166–172.

[40] Y.-H. Ding, P. Zhang, H.-M. Ren, Q. Zhuo, Z.-M. Yang, Y. Jiang, Preparation of graphene/TiO2 anode materials for lithium-ion batteries by a novel precipitation method, Mater. Res. Bull. 46 (12) (2011) 2403–2407.

[41] A. Auer, E. Portenkirchner, T. Götsch, C. Valero-Vidal, S. Penner, J. Kunze-Liebhäuser, Preferentially oriented TiO2 nanotubes as anode material for Li-ion batteries: insight into Li-ion storage and lithiation kinetics, ACS Appl. Mater. Interfaces 9 (42) (2017) 36828–36836.

[42] T. Song, U. Paik, TiO 2 as an active or supplemental material for lithium batteries, J. Mater. Chem. 4 (1) (2016) 14–31.

[43] M. Liu, C. Yan, Y. Zhang, Fabrication of Nb 2 O 5 nanosheets for high-rate lithium ion storage applications, Sci. Rep. 5 (1) (2015) 1–6.

[44] S. Liu, J. Zhou, Z. Cai, G. Fang, A. Pan, S. Liang, Nb2O5 microstructures: a high-performance anode for lithium ion batteries, Nanotechnology 27 (46) (2016) 46LT01.

[45] H. Song, Y. Liu, C. Zhang, C. Liu, G. Cao, Mo-doped LiV 3 O 8 nanorod-assembled nanosheets as a high performance cathode material for lithium ion batteries, J. Mater. Chem. 3 (7) (2015) 3547–3558.

[46] Y.-F. Deng, S.-X. Zhao, Y.-H. Xu, C.-W. Nan, Effect of the morphology of Li–La–Zr–O solid electrolyte coating on the electrochemical performance of spinel LiMn 1.95 Ni 0.05 O 3.98 F 0.02 cathode materials, J. Mater. Chem. 2 (44) (2014) 18889–18897.